Research Square

Preprints are preliminary reports that have not undergone peer review.
They should not be considered conclusive, used to inform clinical practice,
or referenced by the media as validated information.

Host Immune Endotype Determines IL-1β Dominance, Gut Barrier Failure, and Microbiota-Metabolite Circuit Rewiring During Combined Antibiotic and Colitis Injury: Implications for IBD Endotype-Tailored Therapy

Sohini Mukhopadhyay
National Institute of Science Education and Research (NISER)
Kartika Sahu
National Institute of Science Education and Research (NISER)
Debopriya Saha
National Institute of Science Education and Research (NISER)
Palok Aich
palok.aich@niser.ac.in

National Institute of Science Education and Research (NISER)

Research Article

Keywords: Immune bias, gut microbiota perturbation, inflammatory bowel disease, IL-1β dominance, microbe-metabolite network, Lotka-Volterra model

Posted Date: July 11th, 2026

DOI: https://doi.org/10.21203/rs.3.rs-10188173/v1

License: This work is licensed under a Creative Commons Attribution 4.0 International License.
Read Full License

Additional Declarations: No competing interests reported.

Abstract

Purpose

Antibiotics are frequently prescribed during active inflammatory bowel disease (IBD) flares, yet how simultaneous microbial depletion and epithelial injury interact in different immune backgrounds remains unclear. To determine how Th1- versus Th2-biased immunity shapes gut barrier integrity, cytokine architecture, microbiota composition, and metabolic circuits under direct, indirect, and combined gut perturbations.

Methods

Male C57BL/6 and BALB/c mice received a nine-antibiotic cocktail (9AB), dextran sulfate sodium (DSS), or single, sequential, and concurrent 9AB–DSS regimens. Colitis severity, barrier function, and inflammation were assessed. Cecal microbiota, untargeted metabolomics, and phase-plane analysis of pro- versus anti-inflammatory metabolites were integrated.

Results

9AB alone spared the epithelium, whereas DSS induced severe mucosal injury in both strains. Sequential 9AB–DSS regimens attenuated histological damage compared with concurrent treatment, but full barrier restitution after drug withdrawal occurred predominantly in BALB/c mice. In C57BL/6 mice, IL-1β emerged as the dominant mucosal cytokine, coinciding with Proteobacteria expansion and loss of microbial evenness under antibiotic-containing regimens. Metabolomics revealed a Th1-specific arachidonic acid, histidine, and thiamine axis that enriched under combined perturbations. In contrast, BALB/c mice preferentially activated tryptophan, biotin, and glycerophospholipid pathways that supported anti-inflammatory metabolite dominance with phase-plane trajectories returning toward an anti-inflammatory steady state during recovery.

Conclusions

Host immune bias determines whether combined microbial depletion and epithelial injury drive IL 1β-centred metabolic amplification of inflammation or coordinated mucosal recovery. The arachidonic–histidine–thiamine circuit in Th1-biased hosts and the tryptophan–biotin–glycerophospholipid circuit in Th2-biased hosts represent candidate targets for immune endotype-tailored therapeutic strategies in IBD.

Introduction

Antibiotics are prescribed to more than 50% of IBD patients per year during active mucosal inflammation, yet the consequences of combining broad-spectrum microbial depletion with ongoing epithelial injury remain poorly defined [1, 2].This clinical scenario is mechanistically distinct from antibiotic exposure in the absence of gut inflammation: active colitis simultaneously disrupts the epithelial barrier, activates mucosal immune pathways, and remodels the gut microbiota, creating a biological context in which the effects of antibiotic-driven microbial depletion are likely to differ fundamentally from those observed in healthy hosts. Understanding whether and under what host immune conditions, antibiotic exposure during a flare promotes recovery or perpetuates inflammation has direct implications for clinical decision-making in IBD.

The intestinal mucosa maintains homeostasis through continuous bidirectional communication among the gut microbiota, the epithelial barrier, and the mucosal immune system [3]. Microbial communities shape host immunity through pattern-recognition receptor signaling and through metabolites such as short-chain fatty acids, secondary bile acids, and tryptophan derivatives that regulate epithelial integrity and immune-cell differentiation [4–8]. When this equilibrium is disrupted, barrier permeability increases, microbial products translocate beyond the gut lumen, and self-reinforcing inflammatory circuits are engaged that can drive chronic mucosal disease [9]. Inflammatory bowel disease (IBD) is a major clinical consequence of sustained gut ecosystem failure and affects more than 6.8 million people worldwide [2, 10] .

A common but underexplored clinical scenario in IBD is exposure to antibiotics during active mucosal inflammation. [11, 12]. Broad-spectrum antibiotics directly deplete commensal microbial communities and disrupt colonization resistance and microbial metabolic capacity, whereas dextran sulphate sodium (DSS)-induced colitis primarily injures the intestinal epithelium, with microbial remodeling occurring as a downstream consequence. [13, 14]. These perturbations therefore differ in their primary site of action: antibiotics represent a direct perturbation of the gut microbiota, whereas DSS represents an indirect perturbation mediated through epithelial damage [15]. Although each type of insult has been studied separately, the biological consequences of combining microbial depletion with ongoing epithelial injury remain insufficiently defined [16, 17].

This question is especially important because the outcome of gut perturbation is likely to depend not only on the nature of the insult but also on host immune context. Prior work from this group showed that individual antibiotic agents and DSS produce immune bias-dependent dysbiotic signatures in Th1-biased C57BL/6 and Th2-biased BALB/c mice, with greater Proteobacteria expansion, stronger inflammatory tone, and poorer microbial restoration in C57BL/6 mice, whereas BALB/c mice display greater recovery capacity across perturbation conditions. Large-scale human multi-omics studies in IBD have similarly shown that loss of short-chain fatty acid-producing taxa and depletion of bile acid metabolism are associated with disease activity. However, it remains unknown whether these microbial and metabolic functions are differentially preserved or lost when direct and indirect perturbations occur together, and whether host immune polarization determines that outcome [15]. This Th1/Th2 dichotomy in mice approximates, albeit imperfectly, the immunological heterogeneity of human IBD, where IL-1β-high,

inflammasome-active endotypes have been associated with steroid-refractory disease and distinct microbiome signatures in multi-omics cohorts [18, 19]

The present study was designed to address this gap by systematically exposing C57BL/6 and BALB/c mice to a nine-antibiotic cocktail (9AB), DSS, and all single, sequential, concurrent, and recovery regimens derived from these two perturbations. This design was intended to model clinically relevant scenarios in which antibiotic exposure occurs before, during, or after active epithelial injury. To resolve how immune bias shapes these responses, histopathology, intestinal permeability, expanded cytokine profiling, 16S rRNA microbiome analysis, untargeted LC-MS/MS metabolomics, pathway enrichment, and microbe–metabolite network analysis were integrated. The central hypothesis was that immune polarization determines not only the magnitude but also the qualitative architecture of the response to combined gut perturbation, such that Th1-biased hosts would preferentially enter a metabolically amplified pro-inflammatory state, whereas Th2-biased hosts would more effectively engage reparative microbe–metabolite programs that support barrier recovery. By identifying immune endotype-specific metabolic circuits that determine recovery versus inflammatory persistence, we aim to provide a mechanistic framework for rationalizing antibiotic timing and adjunctive metabolic therapy in IBD patients stratified by inflammatory endotype.

Materials and Methods

Ethics Statement and Animal Husbandry

All animal procedures were approved by the Institutional Animal Ethics Committee (IAEC, CPCSEA Registration No. 1634/GO/ReBi/S/12/CPCSEA; protocol NISER/SBS/IAEC/AH-186) and conducted in accordance with approved guidelines. Specific pathogen-free male C57BL/6 and BALB/c mice (6 to 8 weeks old, 18 to 22 g) were obtained from the in-house facility at NISER. Mice were co-housed by strain in polysulfone cages with sterile corncob bedding under a 12:12 h light-dark cycle (24 +/- 3 degrees C, 55 +/- 5% humidity) with standard pelleted chow and autoclaved water ad libitum.

Experimental Design and Treatment

The study used two mechanistically distinct perturbation agents: a nine-antibiotic cocktail (9AB) as a direct perturbation acting primarily on the gut microbial community [11, 12], and dextran sulfate sodium (DSS) as an indirect perturbation targeting the intestinal epithelium [13, 14]. The experimental setup has single-agent, sequential, concurrent, and recovery regimens for both strains, with untreated controls Fig. 1.

DSS (M.W.-50kDa, Fisher Scientific) was dissolved at 2.5% (w/v) in autoclaved water and renewed three times per week [20]. The 9AB cocktail was administered in autoclaved drinking water at the following concentrations: neomycin (100 microg/ml), streptomycin (50 microg/ml), penicillin (100 microg/ml), vancomycin (50 microg/ml), metronidazole (100 microg/ml), bacitracin (1 mg/ml), ciprofloxacin (125

microg/ml), ceftazidime (100 microg/ml), and gentamycin (170 microg/ml), selected to achieve broad-spectrum depletion across all major bacterial phyla [21]. Treatment groups are described in Fig. 1.

Sample Collection

Six animals per group were sacrificed at days 0, 7, and 15 by CO_2 inhalation (confirmed within 2.5 min). Humane endpoints for early removal included rectal prolapse, greater than 15% body weight loss, or signs of clinical distress. Cecal contents were snap-frozen in liquid nitrogen and stored at -80 degrees C. Colon tissue was divided into aliquots for RNA extraction (RNAlater, -20 degrees C), histopathology (4% paraformaldehyde, 72 h, room temperature), and protein analysis (snap-frozen, -80 degrees C). Serum was isolated from whole blood by centrifugation at 1,600 x g for 10 min at 4 degrees C and stored at -20 degrees C.

Sample sizes of n = 6 per group per time point were determined on the basis of our prior studies demonstrating that this number achieves 80% power to detect a 2-fold difference in cytokine mRNA expression ($\alpha = 0.05$, two-tailed). For metabolomics and microbiome analyses, n = 6 is consistent with published discovery-level studies in experimental colitis and was treated as hypothesis-generating; results will require validation in larger cohorts. No adjustment for multiple comparisons was applied to metabolomics pathway enrichment; impact factor thresholds (> 0.25) were used as an effect-size filter in lieu of FDR correction, as is standard practice in untargeted metabolomic pathway analysis.

Physiological Parameters and Intestinal Permeability

Body weight and water intake were recorded daily. Colon length was measured post-mortem and cecal index was calculated as cecal weight divided by body weight. Intestinal permeability was assessed by oral FITC-dextran gavage (44 mg/100 g body weight, 100 mg/ml in PBS; Sigma-Aldrich Cat# F7250) following overnight fasting with bedding removal to prevent coprophagy [22]. Blood was collected by cardiac puncture under isoflurane anesthesia, 4 hours post-gavage; serum fluorescence was measured in duplicate at 528/485 nm emission/excitation.

Histopathological Analysis

Paraffin-embedded colon sections (5 microm) were stained with haematoxylin and eosin (H&E) and Alcian blue/PAS and scored in a blinded manner across six parameters: leukocyte density and infiltration extent, epithelial cell number change, goblet cell reduction, cryptitis, erosion, ulceration, crypt irregularity and loss, and villous blunting. Each criterion was scored on a scale of 1 to 5 (Supplementary Table 1); scores were summed per animal. Images were acquired using an inverted microscope (Olympus CKX53).

RNA Extraction and Gene Expression Analysis

Total RNA was extracted from 20 to 25 mg frozen colon tissue using the Qiagen RNeasy Mini Kit (Cat# 74104) and purified by two rounds of LiCl precipitation to eliminate polysaccharides including DSS contamination (full protocol in Supplementary Methods). RNA quality was assessed by NanoDrop 2000 and Qubit 4 fluorometry; integrity was confirmed by Agilent 4200 TapeStation. Complementary DNA was synthesized using the AffinityScript One-Step RT-PCR Kit (Cat# 600559, Agilent). Quantitative RT-PCR was performed on a QuantStudio 7 instrument (Thermo Fisher Scientific) using SYBR Green Master Mix (Cat# A6002, Promega) for a sequence of cycles, a) a cycle for 2 minutes at 92°C to activate DNA polymerase, b) 15 seconds at 92°C for melting of the template, and c) 1 minute at 60°C for primer annealing along with an extension of the chain and detection of the fluorescence for 40 cycles. Target genes were Tnf-alpha, Il-6, Il-17a, Il-1beta, Il-10, Cldn2 and Ocln, normalized to Gapdh and the fold change of the desired gene was calculated relative to the control C_t-value. Primer sequences are provided in Table 1.

Table 1
Primer sequences

Genes specific to	NCBI_ Acc. No.	The sequence of the primer used (5′-3′)
GAPDH	**NM_008084**	**F**: CATCACTGCCACCCAGAAGACTG
		R: ATGCCAGTGAGCTTCCCGTTCAG
TNF-α	**NM_01278601**	**F**: TGCCTATGTCTCAGCCTCTTC
		R: GAGGCCATTTGGGAACTTCT
CLDN-2	**NM_016675**	**F**: AGGACTTCCTGCTGACATCCAG
		R: AATCCTGGCAGAACACGGTGCA
OCLN	**NM_008756**	**F**: GTTGAACTGTGGATTGGCAG
		R: AAGATAAGCGAACCTTGGCG
IL-1β	**NM_008361**	**F**: TGTAATGAAAGACGGCACACC
		R: TCTTCTTTGGGTATTGCTTGG
IL-6	**NM_001314054**	**F**: CTCTGCAAGAGACTTCCATCCAGT
		R: CGTGGTTGTCACCAGCATCA
IL-17a	**NM_010552**	**F**: CAGACTACCTCAACCGTTCCAC
		R: TCCAGCTTTCCCTCCGCATTGA
IL-10	**NM_010548**	**F**: GCTCTTACTGACTGGCATGAG
		R: CGCAGCTCTAGGAGCATGTG

16S rRNA Amplicon Sequencing and Microbiome Analysis

Cecal DNA was extracted using phenol-chloroform-isoamyl alcohol extraction after heat lysis and purified by two-round LiCl precipitation to polysaccharides, including DSS (full protocol in Supplementary Methods). V3-V4 16S rRNA amplicons (primers V3F: 5'-CCTACGGGNBGCASCAG-3'; V4R: 5'-GACTACNVGGGTATCTAATCC – 3') were sequenced on Illumina MiSeq (paired-end 2 x 250 bp; mean depth 500,823 +/- 117,098 reads/sample). More than 90% of the sequences had a Phred quality score above 30 and GC content nearly 40–60%. We removed conserved regions from the paired end reads. Quality-filtered reads were processed through the QIIME pipeline (OTU clustering at 97% identity, taxonomic assignment against the SILVA database; full pipeline in Supplementary Methods) [23]. OTUs present at fewer than 2 counts or in fewer than 20% of samples were removed; data were normalized by total-sum scaling. Microbial evenness at genus level was calculated as the Shannon evenness index:
Evenness Index (E) = $-\backslash\mathrm{varvec}\Sigma\ \mathbf{E_i ln E_i}$
Where,

$\mathbf{E_i}$ = proportion of the individual genus in the total microbial pool.

$\mathbf{lnE_i}$ = natural logarithm of E_i.

$-\backslash\mathrm{varvec}\Sigma$ = negative sum of $\mathrm{E_i lnE_i}$ for an individual in a specific treatment condition.

Untargeted Metabolomics

Serum (50 microl) and cecal content (50 mg) were processed for untargeted LC-MS/MS (full sample preparation in Supplementary Methods). Analysis was performed on a TripleTOF 6600 system (AB SCIEX) in positive and negative ionization modes (m/z 50 to 1,000; 0.5 ml/min; 5 microl injection) using water/methanol with 0.1% formic acid as mobile phases. Metabolite identification was performed using MS-DIAL against the MassBank/NIST spectral library. Compounds consistently detected in both serum and cecal fractions were designated as circulatory metabolites representing gut microbe-derived compounds with capacity for systemic circulation. Pathway enrichment analysis was performed in MetaboAnalyst 6.0 (KEGG library; hypergeometric test; relative-betweenness centrality for topology; impact factor threshold 0.25) [24].

Microbe-Metabolite Network Analysis

Spearman rank correlations (|r| >= 0.8) between genus-level microbial abundances and circulatory metabolite abundances were used to construct strain-specific microbe-metabolite interaction networks visualized in Cytoscape 3.10.3 [25]. Bipartite condition-pathway networks were assembled by integrating treatment conditions with significantly enriched metabolic pathways; edge color reflected pathway impact factor. Full network construction details are provided in Supplementary Methods.

Descriptive Metabolite Dynamics Modeling

A Lotka-Volterra-type mathematical framework was applied to aggregate serum metabolite data (pro-inflammatory as prey, anti-inflammatory as predator) as a descriptive visualization tool only; it does not constitute an independent experimental result. Parameters were estimated in Python (SciPy; nonlinear least-squares with L2 regularization; coefficients bounded 0 to 100) [26]; phase portraits were generated using the phaseportrait package. Full derivation and code are available at https://github.com/sahukartika/inflammatory-dynamics-model and described in Supplementary Methods.

Results

To assess various degrees of perturbation on host physiology, we used two different perturbing agents: a chemical agent (dextran sodium sulfate, DSS) and a cocktail of nine antibiotics (9AB). DSS activates inflammatory responses in the gut epithelium, which secondarily leads to gut microbial perturbation; accordingly, we designated DSS-induced perturbation as indirect perturbation of the gut microbiota. The 9AB cocktail directly targets and depletes the normal gut flora without requiring an epithelial insult as an intermediate step; we designated this as direct perturbation. We used all possible combinations of direct and indirect perturbation, as single doses and combinatorial doses for 15 days, in both Th1-biased C57BL/6 and Th2-biased BALB/c mice to understand how perturbation strategy controls host physiology, immunity, and metabolism. Building on our prior work demonstrating that individual antibiotic agents and DSS produce immune bias-dependent dysbiotic signatures in these two mouse strains [27], the present study extends that framework by introducing a broader nine-antibiotic cocktail, combinatorial and sequential treatment regimens, and systems-level metabolomics and network analysis to resolve the mechanistic basis of immune bias-dependent resilience versus collapse. The full experimental design is depicted in Fig. 1.

1. Direct Perturbation Spares the Epithelium Whereas Indirect Perturbation Causes Severe Mucosal Injury

To establish the primary structural consequences of each perturbation mode, we performed H&E and Alcian blue/PAS staining of colon sections from all treatment groups in both strains and scored tissue atrophy using the blinded six-criterion system described in Supplementary Table 1. In both C57BL/6 and BALB/c mice, 9AB treatment produced no significant histological abnormality: crypt architecture was intact, goblet cell density was normal, the mucus layer was preserved, and no edema or neutrophil infiltration was detected (Fig. 2B, 2K for C57BL/6; Fig. 2Y, 2AC for BALB/c), confirming that direct microbial depletion alone does not breach the epithelial barrier in either immune background. This is consistent with our prior observation that single antibiotic agents, including the four-antibiotic AVNM cocktail, did not produce significant epithelial injury in either strain [15], and extends that finding to a broader nine-antibiotic regimen.

DSS treatment produced the opposite picture in both strains: extensive ulceration, crypt loss, goblet cell ablation, submucosal edema, and dense neutrophil infiltration (Fig. 2C, 2U), with near-complete loss of

goblet cells and mucus layer integrity confirmed by Alcian blue/PAS staining (Fig. 2L, 2AD). Concurrent 9AB and DSS treatment for 7 days reproduced comparable injury in C57BL/6 (Fig. 2D, 2M) and BALB/c (Fig. 2V, 2AE). Strikingly, sequential administration of 9AB and DSS in either order markedly attenuated epithelial injury in both strains relative to concurrent treatment, with histological appearances approaching untreated controls in C57BL/6 (Fig. 1E, F, N & O) and BALB/c (Fig. 1W, X, AF & AG) mice. So, probably 9AB was contributing a protective role against DSS, whether administered before or after the DSS treatment.

Within the recovery groups, barrier disruption persisted at day 15 in the DSS+H2O group despite DSS withdrawal (Fig. 2H, 2Q for C57BL/6; Fig. 2Z, 2AI for BALB/c), whereas the 9AB&DSS+H2O group showed substantial barrier restitution in both strains (Fig. 2I, 2R for C57BL/6; Fig. 2AA, 2AJ for BALB/c), again indicating protective role of 9AB against DSS. Across all conditions, blinded histopathology scores were consistently and significantly higher in C57BL/6 than BALB/c mice (Fig. 2AK), establishing that Th1 immune bias confers greater epithelial vulnerability to both perturbation modes [15].

2. Systemic Physiology and Gut Barrier Function Confirm Greater Disease Burden in Th1-Biased Mice

Consistent with the histological findings, systemic physiological parameters reflected greater disease severity in C57BL/6 mice across all perturbation conditions. Body weight loss was most pronounced in 9AB + DSS combination groups in both C57BL/6 (Fig. S1A) and BALB/c (Fig. S1B) mice, with decline commencing at DSS treatment onset rather than at antibiotic initiation, confirming that indirect perturbation is the primary driver of systemic physiological deterioration. Post-mortem colon length was shortest in C57BL/6 mice in the 9AB&DSS+H2O group, followed by the 9AB&DSS group, Whereas in the BALB/c 9AB + DSS group had the shortest colon length (Fig. S1C). Cecal index (cecal weight/ body weight) was most elevated in the DSS+9AB group in C57BL/6, followed by 9AB&DSS and 9AB; BALB/c mice showed attenuated cecal enlargement across all conditions (Fig. S1D).

FITC-dextran permeability was highest in the DSS group in C57BL/6 mice, followed by the 9AB&DSS group (Fig. S1E). In BALB/c mice, the highest gut permeability was observed in the DSS-treated group, followed by the DSS+H2O-treated group (Fig. S1E). This is similar to the histopathological where we observed the maximum effect for DSS treatment.

Tight junction proteins such as ZO-1, Occludin, and Claudin-1 1 & 2 play a very crucial role in maintaining the gut barrier integrity of the host [28, 29]. Therefore, we measured the transcription level changes of the genes responsible for maintaining gut integrity. ZO-1, Ocln, and Cldn1 are downregulated genes in leaky gut conditions, whereas Cldn2 is highly expressed in the leaky gut. We observed that Cldn2 was overexpressed in DSS and 9AB&DSS-treated groups in both strains (Fig. 3F), and Ocln was highly downregulated in BALB/c compared to C57BL/6 (Fig. S1G). So, the tight junction genes had a mixed effect on their expression of the disease severity.

3. IL-1β, Not TNFα, Dominates the Colonic Inflammatory Response in C57BL/6 Mice Under Combined Perturbation

Building on the barrier and physiological data, we quantified the transcriptional inflammatory response from colon tissue of both strains using an expanded cytokine panel that added IL-1beta and IL-17 to the TNFα, IFN-gamma, and IL-10 measurements reported in our prior single-perturbation study [15]. We measured mRNA expression of pro-inflammatory TNF-alpha (Fig. 3A), IL-6 (Fig. 3B), IL-17 (Fig. 3C), IL-1β (Fig. 3D), and anti-inflammatory IL-10 (Fig. 3E) from colon tissue of both strains.

In C57BL/6 mice, IL-1β was the overwhelmingly dominant mediator across all perturbation conditions, with fold-change values of 200 to 400 relative to day-0 controls (Fig. 3D, Fig. S2A&C), while TNFα, IL-6, and IL-17 were altered by no more than 2 to 3-fold (Fig. 3A-C). This IL-1beta-centric signature appeared under 9AB alone, DSS alone, and all combination regimens, suggesting it reflects a constitutive feature of Th1-biased inflammatory architecture rather than a response to any specific perturbation trigger. This reveals for the first time that IL-1beta substantially dominates the mucosal inflammatory response in C57BL/6 mice under gut perturbation.

The magnitude of IL-1β induction observed here (200–400-fold) is notable in the context of human IBD, where elevated mucosal IL-1β has been documented in treatment-refractory Crohn's disease and has been proposed as a stratification marker for anti-IL-1 therapy responsiveness [30]. The constitutive nature of this signature across all perturbation types in Th1-biased hosts suggests it reflects host-intrinsic inflammatory architecture rather than a perturbation-specific response, a finding with implications for patient endotyping.

In BALB/c mice, all five cytokines were modulated proportionately and, in a condition, dependent manner without extreme dominance by any single mediator (Fig. 3A-E). Pairwise plots showing that most condition pairs in BALB/c did not reach significant cytokine divergence (Fig. 3A-E). Only the combined 9AB & DSS regimen exceeded the regulatory threshold of the Th2-biased background and elicited significant pro-inflammatory cytokine induction.

4. Direct Perturbation Depletes Microbial Diversity; Immune Bias Determines the Compositional Trajectory

To identify the microbial correlates of the divergent host responses described above, we profiled cecal microbial communities by 16S rRNA sequencing. Baseline phylum-level compositions were broadly similar between C57BL/6 and BALB/c mice at day 0, confirming that post-perturbation differences reflect host-driven responses rather than pre-existing community divergence. Shannon evenness index analysis at genus level confirmed that 9AB caused the greatest reduction in microbial diversity in both strains, followed by DSS+9AB and 9AB + DSS sequential regimens, while DSS alone produced the least diversity reduction across all perturbation conditions, approaching untreated control values in both strains (**Fig. S2C**). This confirms that direct perturbation depletes the microbiota whereas indirect perturbation remodels community composition without equivalent diversity loss, extending our prior single-agent observations [15] to combinatorial regimens.

At the phylum level, C57BL/6 mice showed consistent Proteobacteria expansion under 9AB and DSS+9AB conditions, while BALB/c mice retained Firmicutes-dominated communities across nearly all treatment groups (**Fig. S2A**). The Proteobacteria expansion pattern in C57BL/6 under 9AB is consistent with our prior observations under AVNM [15] and extends them to a broader depletion regimen, reinforcing Proteobacteria expansion as a reproducible dysbiosis signature of Th1-biased hosts under direct perturbation. At the genus level, stacked abundance profiles (**Fig. S3A-B**) showed that C57BL/6 mice expanded Orchobactum in 9AB and DSS+9AB treatment, and expanded Ruminococcus in DSS treatment. An interesting observation is, in case of both strains the 9AB&DSS combined treatment causes expansion of Clostridium, but in case of BALB/c the abundance went down again after 7 days water treatment. But in case of C57BL/6 it kept expanding (**Fig. S3A-B**). Pairwise fold-change comparisons quantifying how treatment conditions differed in their genus-level outcomes across all possible condition pairs are provided in (**Fig. S3C-D**).

5. Pro-Inflammatory and Anti-Inflammatory Metabolite Dominance in C57BL/6 and BALB/c Mice Captured by Phase-Plane Analysis

To provide a descriptive visualization of the temporal relationship between the measured pro- and anti-inflammatory metabolite pools, we applied a Lotka-Volterra-type mathematical framework to the aggregate LC-MS/MS data as a descriptive tool. Serum metabolites were classified as pro-inflammatory or anti-inflammatory based on published literature (Supplementary Table 2 for C57BL/6 and Supplementary Table 3 for BALB/c), and aggregate abundance sums within each category served as state variables. The framework is applied strictly as a graphical representation of the measured metabolite data; it does not constitute an independent experimental result.

In case of BALB/c, the stable steady state is more towards Y-axis then C57BL/6 in case of control condition, which shows its natural tendency of higher anti-inflammatory response (Fig. 4A, Fig. 5A). In both strains, 9AB and DSS treatment induced pro-inflammatory response, which was observed by their shifted stable steady state towards X-axis (Fig. 4B-C, Fig. 5B-C). But in case of recovering conditions (9AB+H2O and DSS+H2O), BALB/c could recover better then C57BL/6 (Fig. 4E-F, Fig. 5E-F). It might be due to their different immune polarization.

This framework provides an intuitive visual summary of whether a host's metabolite landscape is trending toward pro- or anti-inflammatory dominance over time, information not readily extracted from standard pathway heatmaps, and reveals that Th2-biased hosts possess a wider anti-inflammatory basin of attraction under the perturbation conditions tested.

6. Pathway Enrichment and Connectome Analysis Reveal Strain-Specific Metabolic Rewiring

To determine which metabolic pathways were significantly altered under each perturbation condition and how they differed between strains, we performed pathway enrichment analysis on the untargeted LC-MS/MS metabolite data using MetaboAnalyst 6.0 with the KEGG pathway library (impact factor > 0.25). Bipartite condition-pathway networks constructed for C57BL/6 (Fig. 6B) and BALB/c (Fig. 6C)

illustrate which pathways were enriched under each perturbation condition in each strain. In C57BL/6 mice, antibiotic-containing conditions consistently enriched arachidonic acid metabolism (impact factor 0.30, absent from BALB/c under all conditions), histidine metabolism (peak impact factor 0.59 under 9AB + DSS and sequential conditions), and thiamine metabolism (impact factor 0.67, the highest in the entire dataset, also absent from BALB/c). This circuit is mechanistically coherent with the IL-1β dominance described above: arachidonic acid metabolites (prostaglandin E2, leukotriene B4) amplify NLRP3 inflammasome activation, histamine potentiates mast cell-driven IL-1β release via H3 receptor signaling, and thiamine deficiency impairs colonocyte oxidative phosphorylation, sustaining rather than resolving the inflammatory state. Butanoate (butyrate) metabolism appeared across multiple conditions in C57BL/6 but was enriched in fewer conditions in BALB/c. In BALB/c mice, the condition-pathway network showed distinctive pathways do not present in C57BL/6, including vitamin B6 metabolism across seven conditions, glycerophospholipid metabolism in control and combined perturbation conditions, and tryptophan metabolism with consistently higher impact factors (0.25 to 0.46) than in C57BL/6 (0.25 to 0.33). Temporal resolution of pathway perturbation is provided by pathway impact heatmaps at days 7 and 14 for each strain (Fig. 6D-E for C57BL/6; Fig. 6F-G for BALB/c). Notably, during the recovery phase, C57BL/6 showed a dramatically higher number of enriched pathways in the combined 9AB&DSS+H2O condition (13 pathways, including the TCA cycle, riboflavin, pentose phosphate, and glyoxylate metabolism), indicative of broad uncoordinated metabolic disruption rather than targeted repair, while BALB/c showed only 5 enriched pathways in the same condition and additionally activated biotin metabolism during both DSS+H2O and DSS_9AB+H2O recovery, a reparative signature associated with fatty acid synthesis and colonocyte membrane renewal.

To understand how microbial compositional changes and metabolite perturbations were integrated at a systems level, we constructed microbe-metabolite interaction networks from Spearman rank correlations (|r| >= 0.8) between genus-level microbial abundances and circulatory metabolite abundances (Fig. S4 for C57BL/6 and Fig. S5 for BALB/c). Key metabolites contributing to the most significantly altered pathways within each strain were identified (Fig S6B for C57BL/6 and Fig S7B for BALB/c) and specific microbial genera relate to overall metabolic pathway alterations in each strain, we mapped the correlated genera to their associated metabolic changes across all conditions for C57BL/6 (Fig. S6A, Fig. S8A-H) and BALB/c (Fig. S7A, Fig. S9A-H), showing how different genera are connected through shared metabolic alterations. Integrated network analysis linking microbial abundances with metabolite profiles revealed immune bias-specific rewiring of host-microbe metabolic

Discussion

Overview

This study examined how host immune bias shapes the consequences of combining broad-spectrum microbial depletion with epithelial injury in experimental colitis [15]. By jointly varying the mode (direct versus indirect) and timing (single, sequential, concurrent, and recovery) of gut perturbations in Th1-biased C57BL/6 and Th2-biased BALB/c mice and integrating histopathology, barrier function, an

expanded cytokine panel, microbiome profiling, metabolomics, and microbe–metabolite networks, several mechanistic themes emerged. First, antibiotic timing relative to epithelial damage determines whether combined perturbation exacerbates or attenuates mucosal injury, and this effect is strongly conditioned by immune endotype. Second, IL-1β, rather than TNF-α, dominates the colonic inflammatory response to combined perturbation in C57BL/6 mice, defining a distinctive cytokine architecture. Third, strain-specific metabolic circuits—an arachidonic acid–histidine–thiamine axis in C57BL/6 and a tryptophan–biotin–glycerophospholipid axis in BALB/c—link immune bias to divergent trajectories of barrier failure versus repair. Together, these data support an endotype-based framework in which the same antibiotic exposure may have fundamentally different outcomes depending on host immune polarization.

Human IBD Omics Contextualization:

The Th1-specific arachidonic acid–histidine–thiamine circuit identified here maps onto molecular features documented in human IBD multi-omics cohorts. In the HMP2/IBDMDB study by Lloyd-Price et al [18]. Crohn's disease patients showed elevated arachidonic acid metabolism and depleted tryptophan pathway activity compared with controls, mirroring the C57BL/6 versus BALB/c divergence observed here. The tryptophan–biotin–glycerophospholipid axis enriched in BALB/c mice during recovery resembles the metabolic signature associated with mucosal healing in ulcerative colitis patients reported by Franzosa et al [31], where tryptophan pathway activity and short-chain fatty acid-linked metabolites were enriched in patients achieving clinical remission. IL-1β dominance in C57BL/6 mice is consistent with single-cell transcriptomic data from human IBD biopsies identifying an NLRP3-active, IL-1β-high macrophage subpopulation enriched in steroid-refractory disease. While causal equivalence between mouse immune endotypes and human IBD subtypes cannot be assumed, these parallels strengthen the translational relevance of the circuits identified and suggest that stratifying IBD patients by IL-1β status and tryptophan pathway activity may help predict antibiotic responsiveness and mucosal recovery capacity [32, 33]

Antibiotic Timing and Immune Context Jointly Determine Whether Combined Perturbation Is Protective or Harmful

The histological and permeability data establish that sequential antibiotic treatment attenuates DSS-driven mucosal injury regardless of order, while concurrent treatment does not, and that this protection is more functionally complete in BALB/c than in C57BL/6. This finding has direct clinical relevance given that antibiotics are prescribed to over 50 percent of IBD patients per year during active mucosal inflammation [34]. The present data demonstrate that it is: in Th2-biased BALB/c mice, sequential antibiotic treatment followed by recovery allows near-complete mucosal restitution, while in Th1-biased C57BL/6 mice, DSS withdrawal alone fails to restore barrier integrity regardless of antibiotic timing. The persistent IL-1β -driven inflammatory state, not the perturbation itself, is the primary obstacle to recovery in Th1-biased hosts, a conclusion supported by the pathway data showing that C57BL/6 mice fail to activate reparative biotin and glycerophospholipid metabolism during recovery while BALB/c mice do.

From a clinical standpoint, these data suggest that the sequencing of antibiotic therapy relative to active mucosal injury, not merely the choice of antibiotic agent, may influence outcome in a manner contingent on the patient's inflammatory endotype. Patients with IL-1β-high, arachidonic acid-enriched profiles may not benefit from concurrent antibiotic–anti-inflammatory regimens in the same way as those with tryptophan-enriched, reparative metabolic profiles. Prospective stratification of IBD patients by mucosal IL-1β levels or serum tryptophan to kynurenine ratios before antibiotic prescription could provide a testable clinical framework derived from these experimental findings.

IL-1β Dominance Under Combined Perturbation: A New Discovery Through Expanded Cytokine Profiling

The 200 to 400-fold IL-1β induction in C57BL/6 mice across all perturbation conditions, dwarfing TNF-alpha, IL-6, and IL-17 which changed by no more than 2 to 3-fold, is a finding enabled by the expanded cytokine panel that added IL-1β and IL-17 to the measurements reported in our prior single-perturbation study [15]. IL-1β production via the NLRP3 inflammasome is activated by commensal-derived pathogen-associated molecular patterns and damage-associated molecular patterns from DSS-injured epithelium [35], and the constitutive appearance of this signature under every perturbation type suggests it reflects a host-intrinsic property of Th1-biased inflammatory architecture. The pathway data mechanistically connect this cytokine finding to specific metabolic circuits: arachidonic acid metabolism, absent from BALB/c under all conditions but present across six conditions in C57BL/6, generates prostaglandin E2 and leukotriene B4, which amplify IL-1β signaling through cAMP and NF-kappaB pathways respectively [36, 37]. This creates a self-reinforcing lipid-cytokine loop in which NLRP3-derived IL-1beta activates phospholipase A2 to release arachidonic acid, and the resulting eicosanoids further potentiate IL-1beta production [38–40].

Thiamine Deficiency Links Energy Metabolism Failure to Inflammatory Persistence in Th1-Biased Hosts

Thiamine (vitamin B1) metabolism carried the highest impact factor in the entire dataset at 0.667 and appeared exclusively in C57BL/6 mice across five conditions. Thiamine is the obligate cofactor for pyruvate dehydrogenase and alpha-ketoglutarate dehydrogenase, the enzymes coupling glycolysis to the TCA cycle and sustaining oxidative phosphorylation in colonocytes [41]. The concurrent appearance of TCA cycle disruption (citrate cycle pathway at impact factor 0.29) exclusively in C57BL/6 in the combined 9AB&DSS recovery condition confirms that mitochondrial energy metabolism is compromised precisely when recovery should be occurring. This creates a metabolic environment that sustains rather than resolves inflammation: compromised oxidative phosphorylation in colonocytes impairs epithelial barrier restitution. In contrast, BALB/c mice showed vitamin B6 metabolism across seven conditions instead of thiamine. Vitamin B6 (pyridoxine) is essential for **T cell** activation, proliferation, and differentiation [42], suggesting a fundamentally different metabolic prioritization in Th2-biased hosts.

Thiamine deficiency is increasingly recognized in hospitalized IBD patients, particularly those on prolonged antibiotic therapy or parenteral nutrition. The present data provide a mechanistic basis for this

clinical observation: antibiotic-driven microbial depletion in Th1-biased hosts specifically disrupts thiamine metabolism pathways, compromising colonocyte mitochondrial function at a time when barrier restitution is most critical. This interpretation suggests that thiamine supplementation may be particularly beneficial during antibiotic therapy in IBD patients with Th1-dominant immune profiles, a hypothesis amenable to testing in clinical supplementation trials.

Histidine Metabolism Amplifies Combined Perturbation Injury in C57BL/6 Mice

Histidine metabolism showed the highest condition-specific impact factors in C57BL/6, peaking at 0.59 under the sequential and combined 9AB and DSS conditions, consistently exceeding the maximum values observed in BALB/c (0.50). Histidine is the direct precursor of histamine, which activates H1 and H2 receptors on mast cells supporting the inflammation[43, 44]. The elevated histidine pathway impact specifically under conditions combining direct microbial depletion with epithelial damage suggests that histamine-mediated amplification contributes to the non-additive injury observed under combined perturbation in C57BL/6. Mast cell-derived histamine also directly potentiates NLRP3 inflammasome assembly through H3 receptor signaling [45], providing an additional mechanistic link between the histidine pathway finding and the IL-1beta dominance established in the cytokine data.

Tryptophan and Biotin Pathways Define a BALB/c Recovery Metabolome Absent from C57BL/6

The most mechanistically informative BALB/c-enriched findings are the tryptophan, biotin, and glycerophospholipid pathways. Tryptophan metabolism appeared in BALB/c with consistently higher impact factors (0.25 to 0.46) than in C57BL/6 (0.25 to 0.33). Tryptophan catabolism through the indole pathway generates aryl hydrocarbon receptor (AhR) ligands that induce colonic regulatory T cells, promote IL-10 and IL-22 secretion from innate lymphoid cells, and reinforce tight junction expression [46–48]. The higher tryptophan pathway impact in BALB/c under antibiotic conditions suggests that the host upregulates its own tryptophan catabolism to compensate for the loss of microbial AhR ligand production, a compensatory host-level response entirely absent in C57BL/6. Biotin metabolism appeared exclusively in BALB/c in three recovery conditions. Biotin drives acetyl-CoA carboxylase for fatty acid synthesis and membrane phospholipid production [49, 50], and its activation during recovery indicates that Th2-biased hosts direct metabolic resources toward membrane lipid synthesis and colonocyte renewal. This is reinforced by the exclusive appearance of glycerophospholipid metabolism in BALB/c in control and combined perturbation conditions, providing the phospholipid precursors required for mucus layer and membrane integrity [51]. The complete absence of these reparative lipid pathways from C57BL/6 under all conditions provides a metabolic explanation for the failure of barrier restitution in Th1-biased hosts that complements the histological and permeability findings.

Dietary strategies that enhance microbial tryptophan catabolism, including tryptophan-enriched diets, indole-producing probiotic strains, or AhR-activating food components, may preferentially benefit IBD

patients with preserved Th2-reparative capacity, whereas patients with Th1-dominant endotypes may require adjunctive IL-1β blockade or thiamine supplementation to unlock similar recovery capacity.

Limitations and Translational Implications

Several limitations should be considered when extrapolating these findings to human IBD. The study used only male mice, so sex-specific effects on immune bias, microbiota composition, and metabolic pathways cannot be assessed. Sample sizes were appropriate for discovery but will require confirmation with larger, prospectively powered cohorts, including adjustment for multiple testing in metabolomic and microbiome analyses. The 9AB cocktail was designed to achieve broad-spectrum depletion and precludes attribution of effects to individual antibiotic classes. The pathway enrichment and network analyses are correlative and based on metabolite membership rather than direct flux measurements; stable isotope tracing and targeted perturbation of the arachidonic, histidine, thiamine, tryptophan, and biotin pathways will be necessary to validate causality.

Despite these limitations, the integrative design provides a mechanistic framework that is readily testable in translational settings. Future work should focus on (i) defining IL-1β-high versus IL-1β-low endotypes in IBD patients and relating them to antibiotic exposure patterns and clinical outcomes, (ii) experimentally modulating the identified metabolic nodes (e.g., cyclooxygenase inhibition, thiamine supplementation, histamine receptor blockade, or enhancement of AhR ligand production) in animal models, (iii) mapping human microbiome–metabolome networks onto the circuits described here. Such efforts could help move antibiotic decision-making and adjunctive metabolic therapies toward a more personalized, immune endotype-tailored approach in IBD, iv) the nine-antibiotic cocktail was designed for broad-spectrum depletion and does not model the targeted antibiotic regimens (e.g., ciprofloxacin/metronidazole, rifaximin) most used in clinical IBD management. Future studies using clinically relevant single-agent or narrow-spectrum regimens will be necessary to determine which components of the arachidonic–thiamine–histidine or tryptophan–biotin circuits are antibiotic-class specific versus host endotype-intrinsic, and v) metabolomics was performed on serum and cecal content; mucosal metabolomics and epithelial flux measurements will be required to confirm that the identified circulating metabolite shifts reflect the intracellular biochemical state of colonocytes during barrier restitution.

Declarations

Competing Interests:

The authors have no financial disclosures or conflicts of interest to declare.

Funding

The institutional funding allocated to PA helped to conduct the present study. The study received no other extramural grant from any funding agency in the public, commercial, or not-for-profit sectors.

Author Contribution

Conceptualization: PA and SM; Methodology: SM, KS, DS & PA,; Writing - original draft preparation: SM, KS; Writing - review and editing: PA & SM; Funding acquisition: PA; Resources: PA; Supervision: PA.

Acknowledgement

We acknowledge the help of the NISER animal house facility & Central instrumentation facility of NISER for the mass spectrometry facility.

Data Availability

All data are either presented as figures or via supplementary tables and figures or Full derivation and code are available at https://github.com/sahukartika/inflammatory-dynamics-model and described in Supplementary Methods.

The Python code used for modeling inflammatory dynamics and generating phase-plane visualizations is publicly available at: (https://github.com/sahukartika/inflammatory-dynamics-model)

References

1. Zeng W, Zhang W-K, Xu D, He K, Huang Y-P, Liu Y-X, et al. Antibiotic consumption of inpatients with inflammatory bowel disease during 2015–2024 and future prediction: Evidence from a general hospital. World J Gastroenterol. 2026;32(4). DOI: 10.3748/wjg.v32.i4.115040
2. Nitzan O. Role of antibiotics for treatment of inflammatory bowel disease. World J Gastroenterol. 2016;22(3):1078.
3. Takiishi T, Fenero CIM, Câmara NOS. Intestinal barrier and gut microbiota: Shaping our immune responses throughout life. Tissue Barriers. 2017;5(4):e1373208.
4. Chu H, Mazmanian SK. Innate immune recognition of the microbiota promotes host-microbial symbiosis. Nat Immunol. 2013;14(7):668–75.
5. Zeng L, Qian Y, Cui X, Zhao J, Ning Z, Cha J, et al. Immunomodulatory role of gut microbial metabolites: mechanistic insights and therapeutic frontiers. Front Microbiol. 2025;16:1675065.
6. Kim CH. Complex regulatory effects of gut microbial short-chain fatty acids on immune tolerance and autoimmunity. Cell Mol Immunol. 2023;20(4):341–50.
7. Ren L, Li M, Wu L, Lin Z, Chen A. Microbial transformation of secondary bile acids: roles in gut ecology and autoimmune diseases. Front Immunol. 2026;17:1769792.
8. Scott SA, Fu J, Chang P V. Microbial tryptophan metabolites regulate gut barrier function via the aryl hydrocarbon receptor. Proc Natl Acad Sci U S A. 2020;117(32):19376–87.

9. Martel J, Chang S-H, Ko Y-F, Hwang T-L, Young JD, Ojcius DM. Gut barrier disruption and chronic disease. Trends Endocrinol Metab. 2022;33(4):247–65.
10. GBD 2017 Inflammatory Bowel Disease Collaborators. The global, regional, and national burden of inflammatory bowel disease in 195 countries and territories, 1990–2017: a systematic analysis for the Global Burden of Disease Study 2017. Lancet Gastroenterol Hepatol. 2020;5(1):17–30.
11. Kim S, Covington A, Pamer EG. The intestinal microbiota: Antibiotics, colonization resistance, and enteric pathogens. Immunol Rev. 2017;279(1):90–105.
12. Rajakovich LJ, Balskus EP. Metabolic functions of the human gut microbiota: the role of metalloenzymes. Nat Prod Rep. 2019;36(4):593–625.
13. Yang C, Merlin D. Unveiling Colitis: A Journey through the Dextran Sodium Sulfate-induced Model. Inflamm Bowel Dis. 2024;30(5):844–53.
14. Nagalingam NA, Kao JY, Young VB. Microbial ecology of the murine gut associated with the development of dextran sodium sulfate-induced colitis. Inflamm Bowel Dis. 2011;17(4):917–26.
15. Mukhopadhyay S, Ray P, Aich P. A comparative analysis of gut microbial dysbiosis by select antibiotics and DSS to understand the effects of perturbation on the host immunity and metabolism. Life Sci. 2023;312:121212.
16. Franzosa EA, Sirota-Madi A, Avila-Pacheco J, Fornelos N, Haiser HJ, Reinker S, et al. Gut microbiome structure and metabolic activity in inflammatory bowel disease. Nat Microbiol. 2018;4(2):293–305.
17. Lloyd-Price J, Arze C, Ananthakrishnan AN, Schirmer M, Avila-Pacheco J, Poon TW, et al. Multi-omics of the gut microbial ecosystem in inflammatory bowel diseases. Nature. 2019;569(7758):655–62.
18. Lloyd-Price J, Arze C, Ananthakrishnan AN, Schirmer M, Avila-Pacheco J, Poon TW, et al. Multi-omics of the gut microbial ecosystem in inflammatory bowel diseases. Nature. 2019;569(7758):655–62.
19. Franzosa EA, Huang K, Meadow JF, Gevers D, Lemon KP, Bohannan BJM, et al. Identifying personal microbiomes using metagenomic codes. Proceedings of the National Academy of Sciences. 2015;112(22). DOI: 10.1073/pnas.1423854112
20. Mukhopadhyay S, Ray P, Aich P. A comparative analysis of gut microbial dysbiosis by select antibiotics and DSS to understand the effects of perturbation on the host immunity and metabolism. Life Sci. 2023;312:121212.
21. Bollenbach T. Antimicrobial interactions: mechanisms and implications for drug discovery and resistance evolution. Curr Opin Microbiol. 2015;27:1–9.
22. Jensen T, Kiersgaard M, Sørensen D, Mikkelsen L. Fasting of mice: a review. Lab Anim. 2013;47(4):225–40.
23. Caporaso JG, Kuczynski J, Stombaugh J, Bittinger K, Bushman FD, Costello EK, et al. QIIME allows analysis of high-throughput community sequencing data. Nat Methods. 2010;7(5):335–6.
24. Pang Z, Lu Y, Zhou G, Hui F, Xu L, Viau C, et al. MetaboAnalyst 6.0: towards a unified platform for metabolomics data processing, analysis and interpretation. Nucleic Acids Res. 2024;52(W1):W398–406.

25. Shannon P, Markiel A, Ozier O, Baliga NS, Wang JT, Ramage D, et al. Cytoscape: A Software Environment for Integrated Models of Biomolecular Interaction Networks. Genome Res. 2003;13(11):2498–504.
26. Virtanen P, Gommers R, Oliphant TE, Haberland M, Reddy T, Cournapeau D, et al. SciPy 1.0: fundamental algorithms for scientific computing in Python. Nat Methods. 2020;17(3):261–72.
27. Mukhopadhyay S, Saha S, Chakraborty S, Prasad P, Ghosh A, Aich P. Differential colitis susceptibility of Th1- and Th2-biased mice: A multi-omics approach. PLoS One. 2022;17(3):e0264400.
28. Chelakkot C, Ghim J, Ryu SH. Mechanisms regulating intestinal barrier integrity and its pathological implications. Exp Mol Med. 2018;50(8):1–9.
29. Luettig J, Rosenthal R, Barmeyer C, Schulzke JD. Claudin-2 as a mediator of leaky gut barrier during intestinal inflammation. Tissue Barriers. 2015;3(1):1–2.
30. Aggeletopoulou I, Kalafateli M, Tsounis EP, Triantos C. Exploring the role of IL-1β in inflammatory bowel disease pathogenesis. Front Med (Lausanne). 2024;11. DOI: 10.3389/fmed.2024.1307394
31. Franzosa EA, Sirota-Madi A, Avila-Pacheco J, Fornelos N, Haiser HJ, Reinker S, et al. Gut microbiome structure and metabolic activity in inflammatory bowel disease. Nat Microbiol. 2018;4(2):293–305.
32. Karataş A, Karakan T, Ekmen N, Ünsal Y, Türkeş GF, Gülbahar Ö, et al. Evaluation of Tryptophan and Its Metabolites in Predicting Disease Activation in Inflammatory Bowel Disease. J Clin Med. 2025;14(3):1016.
33. Shen X, Li Y, Wang D, Sun K. The gut microbiota and its metabolites: novel therapeutic targets for inflammatory bowel disease. Front Immunol. 2025;16. DOI: 10.3389/fimmu.2025.1690279
34. Zeng W, Zhang W-K, Xu D, He K, Huang Y-P, Liu Y-X, et al. Antibiotic consumption of inpatients with inflammatory bowel disease during 2015–2024 and future prediction: Evidence from a general hospital. World J Gastroenterol. 2026;32(4):115040.
35. Aggeletopoulou I, Kalafateli M, Tsounis EP, Triantos C. Exploring the role of IL-1β in inflammatory bowel disease pathogenesis. Front Med (Lausanne). 2024;11. DOI: 10.3389/fmed.2024.1307394
36. Diaz MF, Li N, Lee HJ, Adamo L, Evans SM, Willey HE, et al. Biomechanical forces promote blood development through prostaglandin E2 and the cAMP-PKA signaling axis. J Exp Med. 2015;212(5):665–80.
37. Das UN. Essential Fatty Acids and Their Metabolites in the Pathobiology of Inflammation and Its Resolution. Biomolecules. 2021;11(12). DOI: 10.3390/biom11121873
38. Dennis EA, Norris PC. Eicosanoid storm in infection and inflammation. Nat Rev Immunol. 2015;15(8):511–23.
39. Sheppe AEF, Edelmann MJ. Roles of Eicosanoids in Regulating Inflammation and Neutrophil Migration as an Innate Host Response to Bacterial Infections. Infect Immun. 2021;89(8). DOI: 10.1128/IAI.00095-21
40. Wen FQ, Watanabe K, Yoshida M. Eicosanoid profile in cultured human pulmonary artery smooth muscle cells treated with IL-1β and TNFα. Prostaglandins Leukot Essent Fatty Acids.

1998;59(1):71–5.
41. Kerns JC, Gutierrez JL. Thiamin. Adv Nutr. 2017;8(2):395–7.
42. Bargiela D, Cunha PP, Veliça P, Foskolou IP, Barbieri L, Rundqvist H, et al. Vitamin B6 Metabolism Determines T Cell Anti-Tumor Responses. Front Immunol. 2022;13:837669.
43. Thangam EB, Jemima EA, Singh H, Baig MS, Khan M, Mathias CB, et al. The Role of Histamine and Histamine Receptors in Mast Cell-Mediated Allergy and Inflammation: The Hunt for New Therapeutic Targets. Front Immunol. 2018;9. DOI: 10.3389/fimmu.2018.01873
44. Moro J, Tomé D, Schmidely P, Demersay T-C, Azzout-Marniche D. Histidine: A Systematic Review on Metabolism and Physiological Effects in Human and Different Animal Species. Nutrients. 2020;12(5). DOI: 10.3390/nu12051414
45. Chen Y, Ma Y, Feng JJ, Wang YH, Li TF, Nurmi K, et al. Histamine H3 Receptor Signaling Regulates the NLRP3 Inflammasome Activation in C2C12 Myocyte During Myogenic Differentiation. Front Pharmacol. 2021;12. DOI: 10.3389/fphar.2021.599393
46. Bansal T, Alaniz RC, Wood TK, Jayaraman A. The bacterial signal indole increases epithelial-cell tight-junction resistance and attenuates indicators of inflammation. Proc Natl Acad Sci U S A. 2010;107(1):228–33.
47. Shen J, Wang Y, Zheng F, Cao S, Lan Q, Xu K, et al. Aryl hydrocarbon receptor regulates IL-22 receptor expression on thymic epithelial cell and accelerates thymus regeneration. NPJ Regen Med. 2023;8(1):64.
48. Hubbard TD, Murray IA, Perdew GH. Indole and Tryptophan Metabolism: Endogenous and Dietary Routes to Ah Receptor Activation. Drug Metab Dispos. 2015;43(10):1522–35.
49. Bunn CR, McNeill JJ, Elkan GH. Effect of biotin on fatty acids and phospholipids of biotin-sensitive strains of Rhizobium japonicum. J Bacteriol. 1970;102(1):24–9.
50. Lee C-K, Cheong H-K, Ryu K-S, Lee J Il, Lee W, Jeon YH, et al. Biotinoyl domain of human acetyl-CoA carboxylase: Structural insights into the carboxyl transfer mechanism. Proteins. 2008;72(2):613–24.
51. Schneider H, Braun A, Füllekrug J, Stremmel W, Ehehalt R. Lipid based therapy for ulcerative colitis-modulation of intestinal mucus membrane phospholipids as a tool to influence inflammation. Int J Mol Sci. 2010;11(10):4149–64.

Figures

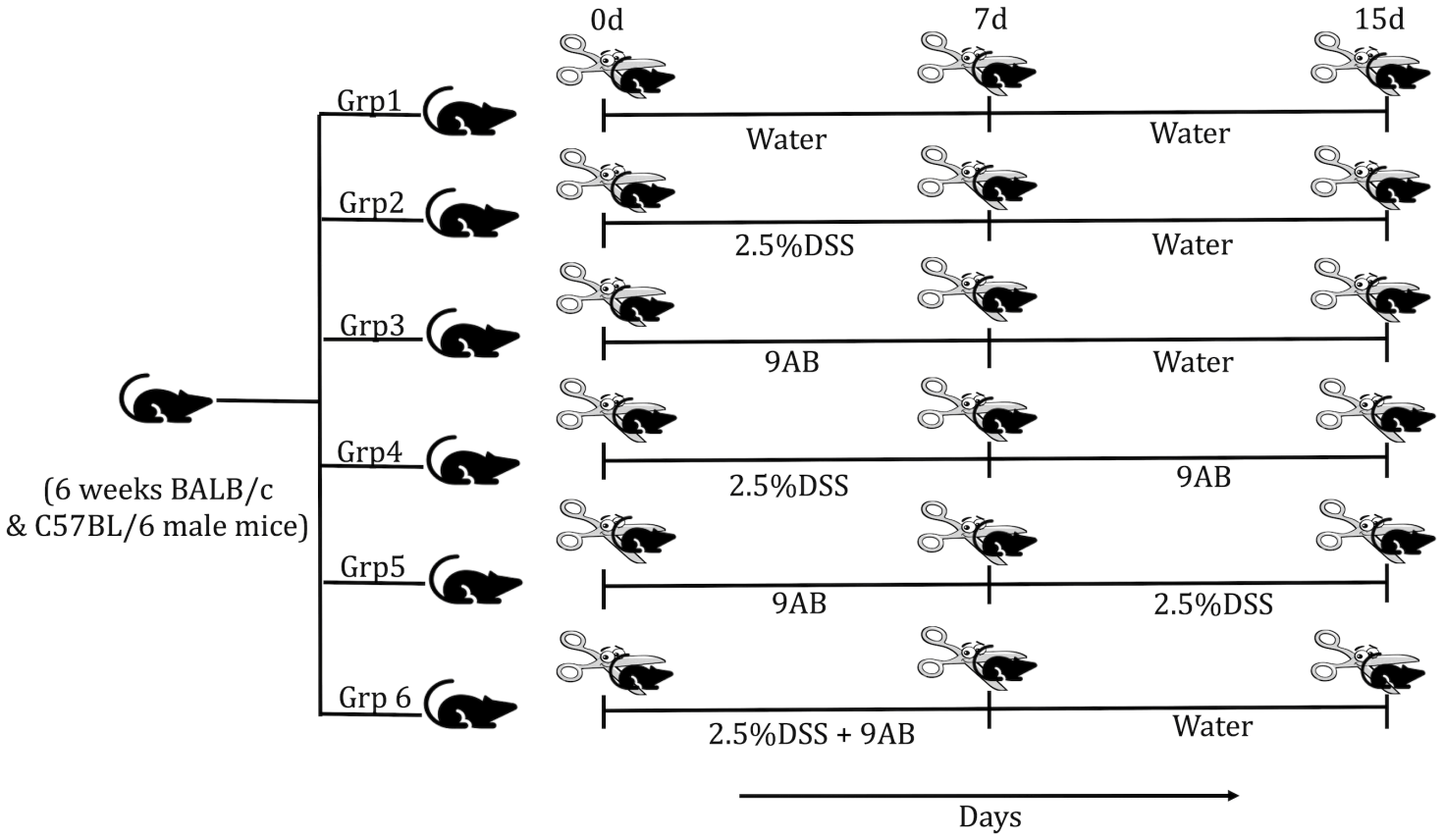


Figure 1

Schematic diagram of the experimental design.

Male C57BL/6 (Th1-biased) and BALB/c (Th2-biased) mice aged 6 to 8 weeks were exposed for 15 days to a nine-antibiotic cocktail (9AB; direct perturbation), dextran sulfate sodium (DSS; indirect perturbation), or all possible single, sequential, and combinatorial regimens, with untreated controls. Treatment groups included: 9AB alone, DSS alone, concurrent 9AB&DSS, sequential 9AB followed by DSS (9AB+DSS), sequential DSS followed by 9AB (DSS+9AB), 9AB followed by water recovery (9AB+H2O), DSS followed by water recovery (DSS+H2O), and concurrent 9AB&DSS followed by water recovery (9AB&DSS+H2O).

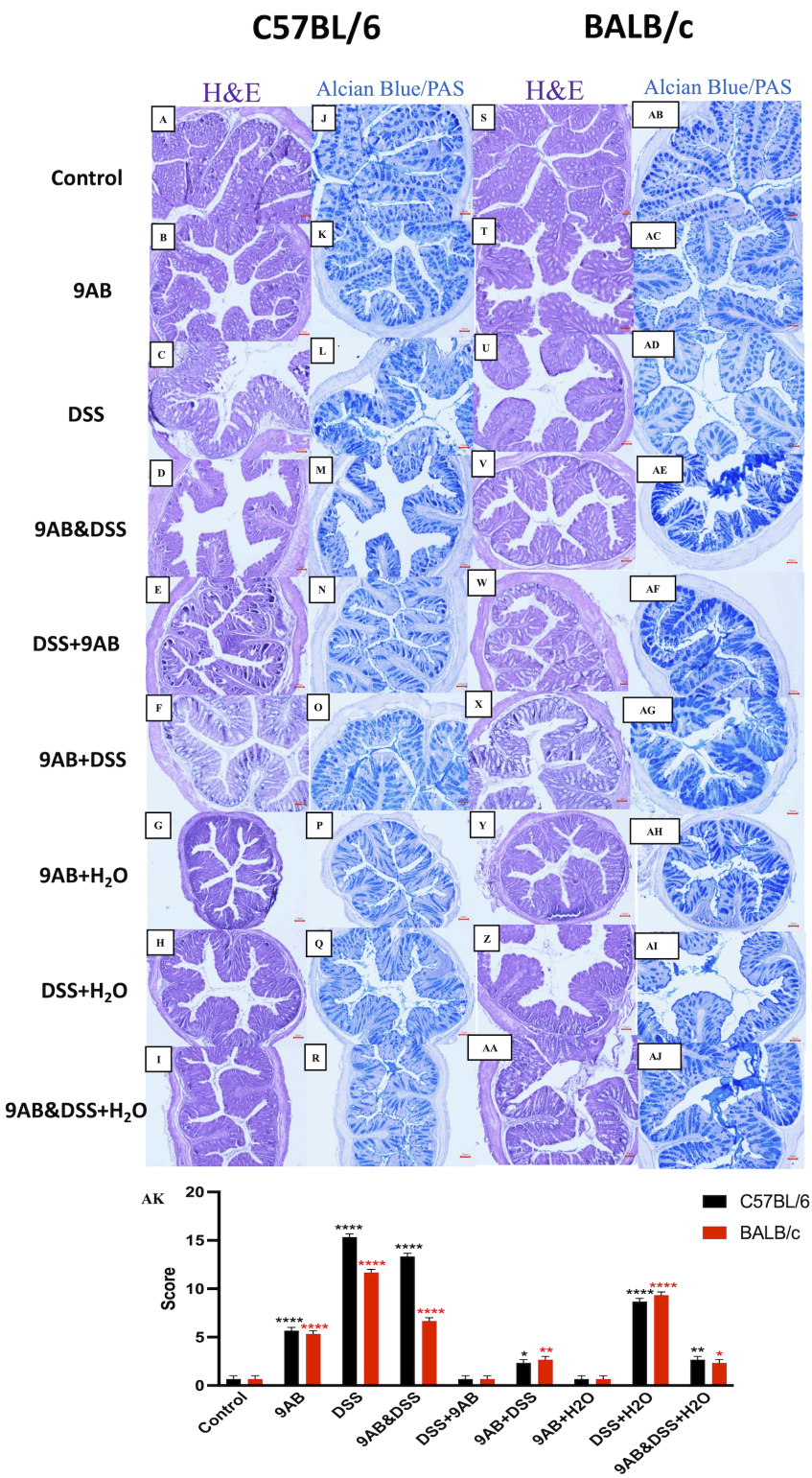


Figure 2

Differential effects of direct, indirect, and a combination of direct and indirect gut microbial perturbations on colon tissue of Th1 and Th2 biased mice.

Due to differential treatment effects, we observed various levels of intestinal tissue atrophy in C57BL/6 (Th1) and BALB/c (Th2) mice. We performed H&E staining (A-I, S-AA) and Alcian Blue/PAS staining (J-R,

AB-AJ) of the colon sections of the control. We treated C57BL/6 and BALB/c mice to measure the changes in epithelium tissue morphology, mucosal architecture, and inflammatory cell infiltration. The image of the histological section of the colon by bright-field microscopy at 20X. We scored the tissue atrophy (AK) using the blind-unbiased method to quantify the changes in intestinal morphology due to perturbation in both Th1 and Th2-biased mice.

We presented data as the means ± SD (n=6). We calculated the statistical significance by comparing the values of the treated groups at various time points with their respective control groups. We used two-way ANOVA followed by the Bonferroni test to determine the significance level of all analyses. * corresponds to P < 0.05, ** corresponds to P < 0.01, *** corresponds to P < 0.001, **** corresponds to P < 0.0001. (For histological analysis, pictures were taken with a magnification of 20X, scale bar 100µm).

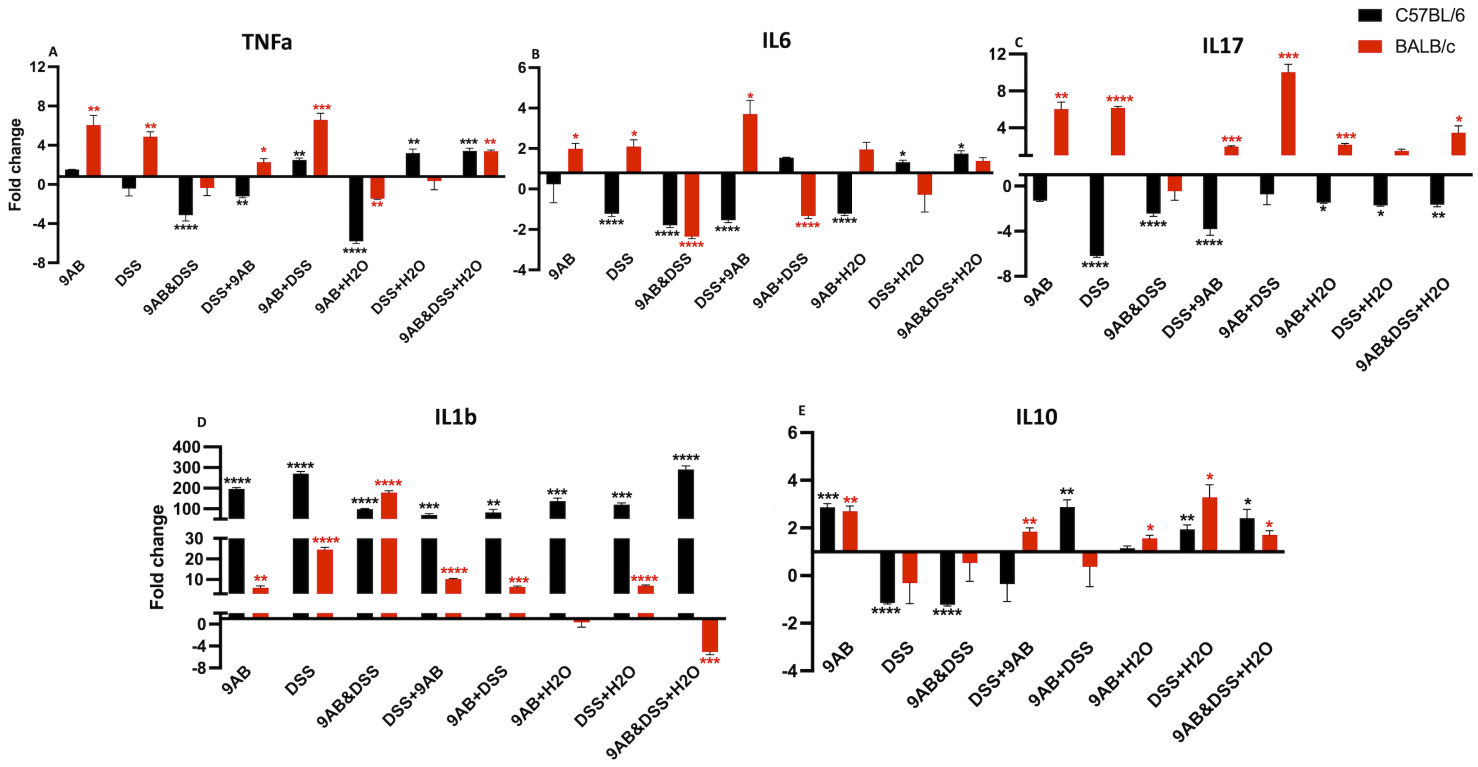


Figure 3

Transcriptional quantification of the inflammatory markers of the colon tissue as a consequence of the various levels of perturbation in both Th1 and Th2-biased mice.

We quantified the changes in the mRNA expression of both pro- and anti-inflammatory genes from the colon tissue. We measured the transcriptional changes of pro-inflammatory TNFa (A), IL6 (B), IL17 (C), IL1b(D) and anti-inflammatory IL10 (E) from both Th1 and Th2 biased mice.

We presented data as means ± SEM (n=3). We performed a t-test to determine the significance level. * Corresponds to P < 0.05, ** corresponds to P <0.01, *** corresponds to P < 0.001, **** corresponds to P <0.0001.

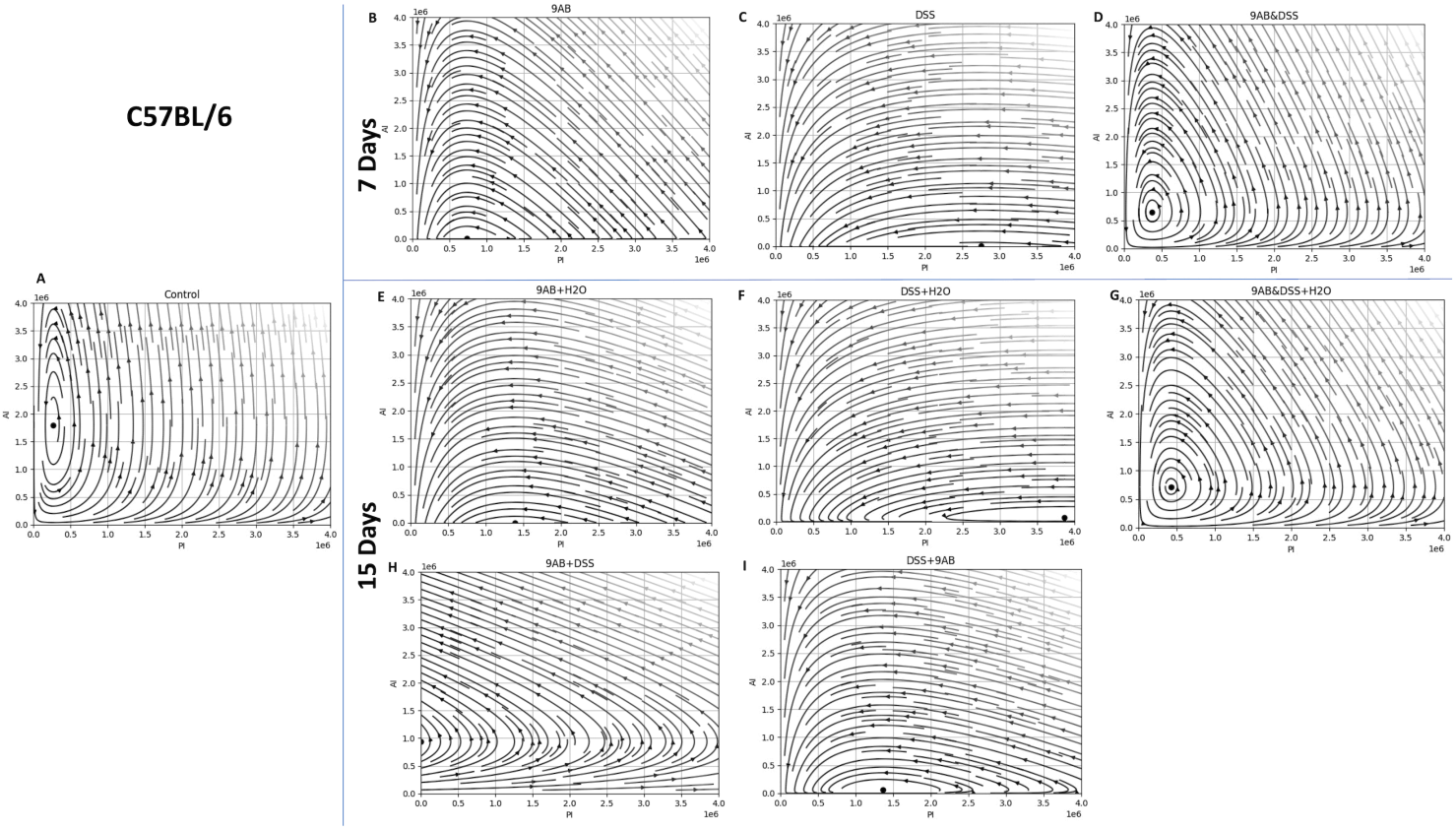


Figure 4

Phase portrait of the pro- and anti-inflammatory microbiota-derived metabolites in C57BL/6 (Th1) mice.

We categorized the significantly altered microbial metabolites as pro (PI) and anti-inflammatory (AI) from all the treatment conditions in C57Bl/6 mice. We employed Nullcline methodology to analyze the expression values of altered metabolites to understand condition-wise inflammatory dynamics of the host due to altered gut microbial compositions. Phase plots depict the dynamic trajectories of pro and anti-inflammatory metabolites in various conditions: control (A), 9AB (B), DSS (C), 9AB&DSS (D), 9AB+H2O (E), DSS+H2O (F), 9AB&DSS+H2O (G), 9AB+DSS (H), DSS+9AB (I) in Th1-biased mice.

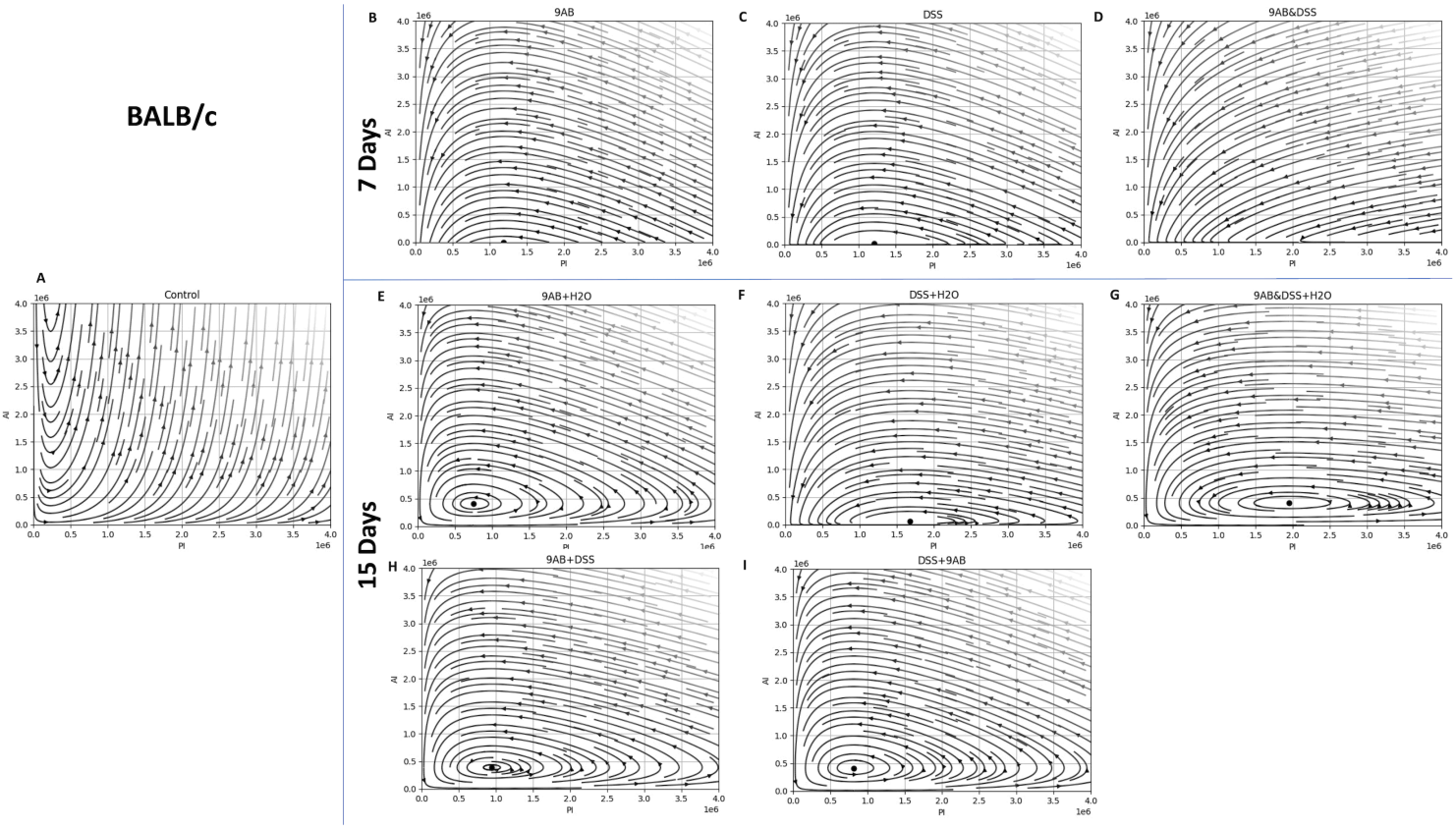


Figure 5

Phase portrait of the pro- and anti-inflammatory microbiota-derived metabolites in BALB/c (Th2) mice.

We categorized the significantly altered microbial metabolites as pro (PI) and anti-inflammatory (AI) from all the treatment conditions in BALB/c mice. We employed Nullcline methodology to analyze the expression values of altered metabolites to understand condition-wise inflammatory dynamics of the host due to altered gut microbial compositions. Phase plane depicts the dynamic trajectories of pro- and anti-inflammatory metabolic profiles in various conditions: control (A), 9AB (B), DSS (C), 9AB&DSS (D), 9AB+H2O (E), DSS+H2O (F), 9AB&DSS+H2O (G), 9AB+DSS (H), DSS+9AB (I) in Th2-biased mice.

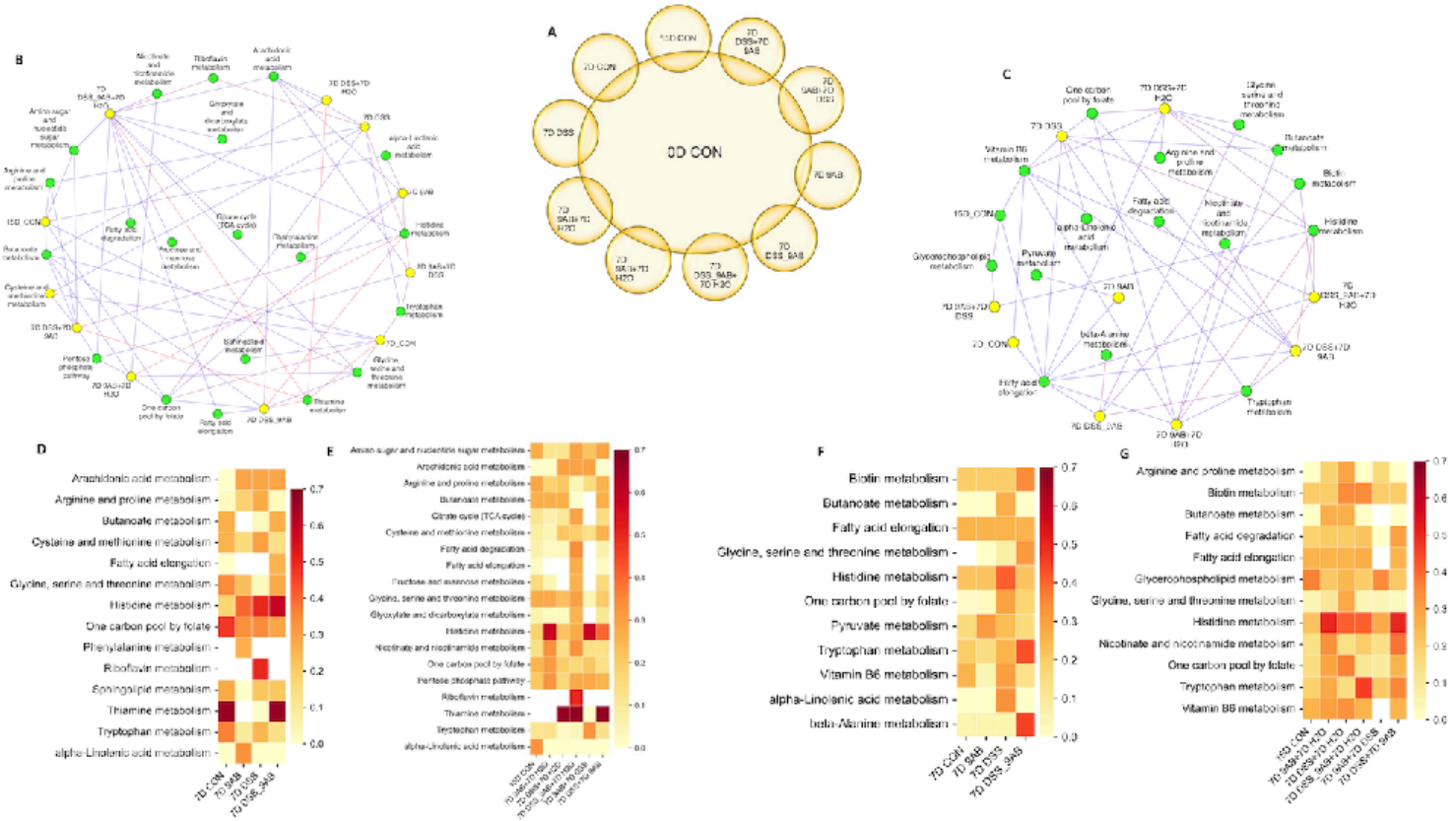


Figure 6

Shared pathways under multiple treatment combinations.

(A) Schematic diagram of finding condition-specific response by comparing each condition with day 0 control. (B, C) Condition pathway network for C57BL/6 and BALB/c mice. (D, E) Pathway abundance heatmap of C57BL/6 mice. (F, G) Pathway abundance heatmap of BALB/c mice.

Supplementary Files

This is a list of supplementary files associated with this preprint. Click to download.

- SupplementaryFiles.docx
- SupplemetaryTable2.xlsx
- SupplemetaryTable3.xlsx
- OnlineGAjpeg.png